Soft Matter

Ridge Localization Driven by Wrinkle Packets

Journal:	*Soft Matter*
Manuscript ID	SM-ART-09-2023-001287.R1
Article Type:	Paper
Date Submitted by the Author:	09-Nov-2023
Complete List of Authors:	Guan, Xianheng; University of Pittsburgh, Department of Mechanical Engineering and Materials Science Nguyen, Nhung; University of Chicago Department of Medicine, Department of Surgery Cerda, Enrique; Universidad de Santiago de Chile, Departmento de Fisica Pocivavsek, Luka; University of Chicago Department of Medicine, Department of Surgery Velankar, Sachin; University of Pittsburgh, Chemical Engineering, Mechanical Engineering and Materials Science

Journal Name

ARTICLE TYPE

Cite this: DOI: 00.0000/xxxxxxxxxx

Ridge Localization Driven by Wrinkle Packets†

Xianheng Guan,[a] Nhung Nguyen,[b,d] Enrique Cerda,[c] Luka Pocivavsek,[d] and Sachin Velankar[a,b]

Received Date
Accepted Date

DOI: 00.0000/xxxxxxxxxx

While buckling is a time independent phenomenon for filaments or films bonded to soft elastic substrates, time evolution plays an important role when the substrate is a viscous fluid. Here we show that buckling instabilities in fluid-structure interactions can be reduced to the analysis of a growth function that amplifies the initial noise characterizing experimental or numerical error. The convolution between a specific growth function and noise leads to natural imperfections that emerge in the form of wave packets with a large scale modulation that can transform into localized structures depending on nonlinear effects. Specifically, we provide an experimental example where these wave packets are amplified into ridges for sufficiently low compression rates or are diluted into wrinkles for high compression rates.

1 Introduction

The deformation of microtubules immersed in intracellular fluids, the motion of cilia on the surface of cells or the displacement of tectonic plates on the surface of the earth, are commonplace examples of fluid-structure interactions at different time and length scales where viscous forces play a dominant role[1–3]. A well-known primary instability leads to sinusoidal undulations or wrinkling if the film or filament bears a compressive strain ε[4–8]. Wrinkles of wavenumber k_m are effective to release the compression of the initial flat state by rotating the structure out of the line of action of viscous forces.

Similar wrinkling instabilities have been extensively studied for the case of a film bonded to a soft elastic substrate[9,10]. Beyond some critical threshold strain ε_c, bending modes can lower the elastic energy more effectively than compressive modes, thus leading to buckling in the form of sinusoidal wrinkles distributed uniformly over the entire surface of the film. Upon further compression, other localized buckling modes such as period-doubled wrinkles or well-separated tall ridges have also been observed and studied[11–16]. Localized buckles can release the local compression of the film more effectively than uniform wrinkles when the stiffness mismatch ratio E/E_s between the elastic film stiffness E and the soft substrate stiffness E_s increases. A more compliant substrate, i.e. a large E/E_s, allows the stiffer film to displace over larger distances, which is essential for localization. Similar sinusoidal or localized instabilities are also observed for inviscid liquid-supported films where gravity or surface tension plays the role of substrate stiffness[17–19].

Analogous localization phenomena were recently reported for films supported on a layer of viscous fluid. Buckles can appear either in the form of uniform wrinkles over the entire film, or well-spaced tall ridges[20–22]. A comprehensive review of the literature on buckling phenomena on viscous substrates is provided in[21]. The mechanism leading to ridge localization in such energy-dissipating systems must however be fundamentally different from the energy-conserving cases from the previous paragraph. While the soft matter community has a sophisticated understanding of buckling in terms of energy, the knowledge of rate effects - which are inevitable for viscous or viscoelastic substrates - is rudimentary. Such substrates fully dissipate mechanical energy, and hence no energy minimizer is available. Instead, for the case of uniform wrinkles, the analysis is similar to instabilities in fluid mechanics (Rayleigh-Taylor, Kelvin-Helmotz, Richtmyer-Meshkov, etc.) where an interface is unstable to small perturbations of wavenumber k and the amplitude grows in the form $A_k e^{S(t,k)}$ with time. The most unstable mode k_m is obtained by maximizing the growth function $S(t,k)$ with respect to k, and the time to observe the instability is dictated by the condition of having the amplitude of order one, $S(t,k_m) \sim \mathcal{O}(\ln(1/A_k))$. Initial perturbations are not expected to play a role in the final shape of the interface when nonlinear effects become dominant. In fact, a great deal of research has been done to understand how the

[a] Department of Mechanical Engineering and Materials Science, University of Pittsburgh, Pittsburgh, PA, USA.
[b] Department of Chemical Engineering, University of Pittsburgh, Pittsburgh, PA, USA.; E-mail: velankar@pitt.edu
[c] Universidad de Santiago de Chile (USACH), Facultad de Ciencia, Departamento de Física, Chile.; E-mail: enrique.cerda@usach.cl
[d] Department of Surgery, University of Chicago, Chicago IL, USA.

† Electronic Supplementary Information (ESI) available: Video Simulation.mp4 shows the evolution of wrinkles at high rate (first part) and low rate (second part). We also provide a detailed theoretical analysis (section 1), a description of the simulation methods (section 2), and correlation function analysis to detect localization and critical strain for buckling (section 3). See DOI: 00.0000/00000000.

final shapes describing bubbles and spikes in Rayleigh-Taylor instability are not dependent on the initial perturbations of the flat interface[23]. Here we show that this scenario is completely different in buckling instabilities resulting from fluid-structure interactions. It is well known that buckling instabilities are extremely sensitive to structural imperfections in real applications, and engineers take careful account of them to avoid failure of a designed structure. These perturbations are attributable to errors during fabrication, the presence of defects, variation of material properties, etc. so that they have an intrinsic random nature and can deviate buckling into unexpected paths. For the case of buckling by viscous forces all these initial imperfections are hidden in the specific values of A_k and the behavior below and near the threshold is expressed by the convolution

$$\psi(x,t) = \mathrm{Re}\left[\int_0^\infty dk A_k e^{ikx} e^{S(t,k)}\right] \quad (1)$$

where ψ represents the out-of-plane deformation of a filament or film. In general, the constants A_k are complex and it is necessary to take the real part of the fourier transform. Wrinkling is predicted by the first order approximation of the integral $\psi \propto A_{k_m} e^{ik_m x} e^{S(t,k_m)} + \text{c.c.}$. However, this paper shows a remarkable result that a second length scale emerges at a second order approximation, assuming that the critical mode is a maximum for the growth function.

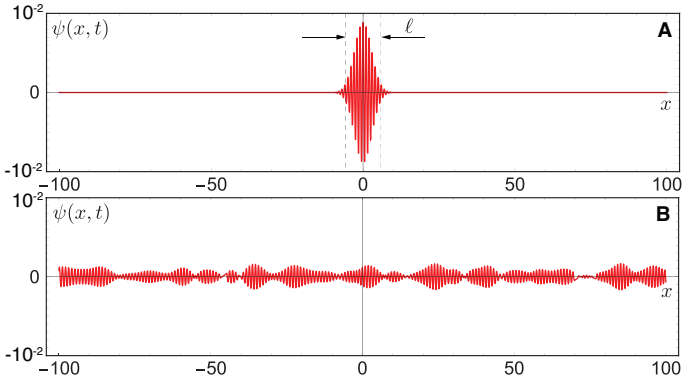

Fig. 1 Surface profiles obtained from Eq. 2 for $k_m = 2\pi$ and $k_0 = 0.5$. A. Convolution for a constant initial amplitude $A_k = 10^{-2}$. The distance between the two vertical dashed lines corresponds to the value $\ell = 4\sqrt{2}/k_0$. B. Convolution for $A_k = 10^{-2} \times p$ where p is a random number between -1 and 1.

Around the maximum the growth function can be approximated as $S(t,k) = S(t,k_m) - (k-k_m)^2/k_0^2$ where $k_0^{-2} = -\partial_k^2 S(t,k)/2|_{k_m}$. It yields

$$\psi(x,t) \approx e^{S(t,k_m)} \mathrm{Re}\left[\int_0^\infty dk A_k e^{ikx} e^{-(k-k_m)^2/k_0^2}\right] \quad (2)$$

The wavenumber k_0 represents the spread of the modes around k_m. The remaining integral is well studied in different fields of physics that account for a range of modes playing a role as the amplitude probability in Quantum Mechanics or surface waves amplitudes in Fluid Mechanics. As known in these other fields, we show that the addition of multiple unstable modes produces a different response than an individual mode. The simple assumption of having a constant real value for the initial perturbations $A_k = A_0$ leads to the classical example describing a wave packet $\psi = A_0 k_0 \sqrt{\pi} e^{S(t,k_m) - k_0^2 x^2/4} \cos(k_m x)$ that is localized along a distance $\sim 1/k_0$ (see Fig. 1A). But there is a whole range of different possibilities depending on the specific statistical distribution of the initial amplitudes A_k. Figure 1B shows the profile when the amplitude follows a random uniform distribution. The amplitude randomness triggers the well-known phenomena of "beating"[24] where competing unstable modes near k_m induce a pulsation of the wrinkled pattern. Thus, the convolution leads to the appearance of natural imperfections at two modes k_m and k_0 and these two modes are available for buckling at threshold. Moreover, the pulsation can be long range, i.e. appears as a long-wavelength modulation of the amplitude for $k_0 \ll k_m$, representing a length-scale that is distinct from the wrinkle wavelength.

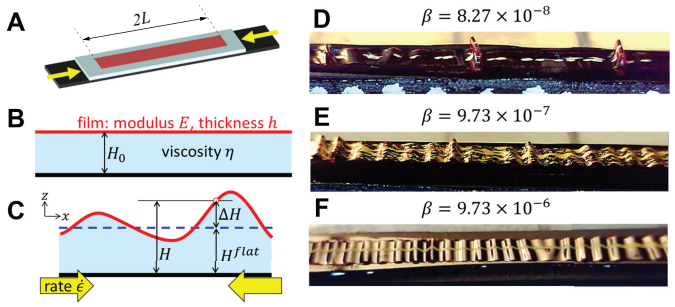

Fig. 2 A. Schematic of the experiment. A film of length $2L$ (orange) is attached to a viscous liquid layer (light blue) coated onto a pre-stretched rubber strip (black). B&C. 2D sketch of geometry before and after buckling. Dashed line indicates film height $H^{flat} > H_0$ if buckling does not happen. D-F. Experimental images at the same compression strain $\varepsilon = 0.14$ and liquid thickness $H_0/h = 31.5$, applied at various rates. β is the dimensionless strain rate defined in the text.

An example of two distinct length scales at the threshold can be seen when a viscous substrate bearing an elastic film is compressed at a constant compression rate[20]. Figure 2 illustrates our experimental setup. A strip of elastic film rests on the surface of a viscous liquid layer, which is itself coated onto a rubber strip being held stretched (Fig. 2A). Releasing the rubber strip imposes compressive stress on the liquid, which in turn compresses the film, causing it to buckle. As described in two recent experimental[21] and numerical studies[22], the buckles can adopt two distinct forms. If the compression rate is relatively large, wrinkles appear uniformly over the entire film (Fig. 2F). If compression rate is relatively small, buckles take on the form of tall and sharply-localized ridges separated by nearly-flat regions (Fig. 2D). Remarkably, wrinkle packets are clearly observed near the threshold (see Fig. 2E) and, unlike in the case of films supported on soft solids where localization is observed far from the onset for wrinkling, ridges localize simultaneously with wrinkles. This implies that localization is not a post-buckling phenomenon. In section 2 we study experimentally and numerically these two length scales in detail and in section 3 we provide a theoretical framework that explains them based on the ideas outlined above on the role of small perturbations may create a long-range modulation. Finally,

we apply the analysis to other configurations in section 4.

2 Experiments and Numerics

Experiments were conducted by placing a 100x8 mm elastic thin film of thickness $h = 25.4$ μm (PET, McMaster-Carr) onto the surface of a polymeric liquid layer of viscosity $\eta \sim 10^6$ Pa.s (polyisobutylene, BASF Oppanol B15), and thickness H_0 ranging from 0.25 to 1.6 mm, which was itself coated onto a prestretched rubber strip (see Fig. 2A). The rubber strip was allowed to unstretch at controlled speed. The liquid layer then induced compression of the film, which buckled. The high viscosity of the fluid ensures that gravity does not play a role in the experiments. Even though the liquid layer is not confined laterally, gravity-driven flow is sufficiently weak that the layer thickness H_0 remains constant for a time scale on the order of one day. Moreover, experiments conducted by hand showed very similar results when tilted at 90 degrees. Simulations were conducted for the geometry of Fig. 2A under plane strain conditions using ABAQUS (see ESI†). Recent works[26–28] have numerically studied a similar configuration but with a viscoelastic substrate exhibiting a rubbery behavior for long times, which plays a role in the final state of the system. Here we enforce that the substrate layer exhibits fluid-like behavior to approximate a Newtonian fluid. Thus the evolution of buckles is entirely determined by a coupling between just two factors: the elasticity of the film and the viscous dissipation in the substrate. The ends of the bottom rubber layer were moved towards each other at fixed velocity to induce compression and buckling. The loading conditions and material properties were selected to ensure that in the rubber layer the compressive strain is $\varepsilon = \dot{\varepsilon}t$ for $t > 0$. The geometry was sufficiently long to approximate infinite film conditions.

For sufficiently long films under plane strain conditions, the mechanics of the film prior to buckling can be captured by three parameters[20]: the non-dimensional strain rate $\beta = (1-\nu^2)\eta\dot{\varepsilon}/E$, where E is the film modulus, ν is the Poisson ratio of the film (set to $\nu = 0.49$ in the numerics); the non-dimensional liquid thickness H_0/h; and the strain $\varepsilon = \dot{\varepsilon}t$. Incidentally the literature under plane strain conditions on thin film buckling sometimes uses the in-plane stiffness $Y = Eh/(1-\nu^2)$ and the bending stiffness $B = Eh^3/12(1-\nu^2)$ (rather than E and h) to characterize the film. In that case, the suitable non-dimensional numbers are $\alpha = \eta\dot{\varepsilon}H_0/Y$, the von Kármán number $N = \sqrt{YH_0^2/B}$, and the strain ε. These latter parameters will be used in our theoretical description. However, β and H_0/h offer the benefit of cleanly separating the material parameters from the geometric ones. Both simulations and experiments spanned the same range of β and H_0/h values although the dimensional values of the material parameters (modulus and viscosity) were orders of magnitude higher in the experiments (Table S1 in the ESI† lists the parameter values used in the simulations). The fact that experiments and simulations produce comparable results confirms that these dimensionless parameters accurately capture the physics.

For quantitative analysis of the simulations, we must isolate film motion that is specifically attributable to buckling. We characterize the film kinematics by the x-displacement $u(x,t)$ of a material point on the film from its initial position, and the height $H(x,t)$ of the film, which is also the liquid layer thickness. If the film stayed flat without buckling, these two quantities would follow (see ESI†):

$$u^{flat} = -\dot{\varepsilon}tx; \quad H^{flat} = H_0/(1-\dot{\varepsilon}t) \tag{3}$$

The first equation states that x-displacement of the film matches that of the bottom rubber layer. The second states that as strain increases, the film rises due to liquid incompressibility, as indicated by the dashed blue line in Fig. 2C. Once the film buckles, the local values of u and H deviate from Eq. (3), and these deviations are written as $\Delta u = u - u^{flat}$ and $\Delta H = H - H^{flat}$. We adopt ΔH (see Fig. 2C) as the definition of the local buckle amplitude.

The red lines in Fig. 3 show the evolution of the non-dimensional amplitude profile $\Delta H/H_0$ for two compression rates (see Supplemental Video†). The onset of buckling is marked by the appearance of non-zero values of $\Delta H/H_0$ at sporadic locations over the film. We found that inter-ridge distance can be identified reliably from the $\Delta\dot{u}$ profiles (i.e. the horizontal film velocity relative to the rubber layer), rather than by measuring the distance between the tallest buckles from the amplitude profiles. The blue lines in Fig. 3 plot these relative x-velocity profiles in non-dimensional form $\Delta\dot{u}/\dot{\varepsilon}H_0$. Remarkably, in the low-rate simulation, (Fig. 3D), while the buckle amplitude is still modest ($\Delta H/H_0 < 0.2$), the $\Delta\dot{u}/\dot{\varepsilon}H_0$ develops a long-wavelength modulation. The modulation is such that the film moves towards locations with relatively large ΔH values; these locations "accumulate film" and grow taller, whereas neighboring regions "supply film" and themselves become flat. With increasing strain, the regions with tall ridges become increasingly narrow, and the velocity profile takes on a sawtooth shape. Yet the wavelength of the modulation and the location of the zeroes in $\Delta\dot{u}/\dot{\varepsilon}H_0$ remain approximately pinned throughout. In contrast, at high-rate (Fig. 3C), $\Delta\dot{u}/\dot{\varepsilon}H_0$ temporarily takes on large values in the vicinity of buckles. But long-range correlations in $\Delta\dot{u}/\dot{\varepsilon}H_0$ do not appear, and subsequently all the buckles increase their amplitude uniformly. The two length scales that characterize the buckling, the wavelength λ, and the inter-ridge distance ℓ, can be estimated readily from the analysis of the spatial autocorrelation functions of $\Delta H/H_0$ and $\Delta\dot{u}/\dot{\varepsilon}H_0$ (see ESI†, section S3). For large values of β or H_0/h, however, the amplitude of the tallest ridges no longer dominates over all the others, and hence ℓ is not reported. Figure 4 compares numerical and experimental results for the wavelength and inter-ridge distance. In summary, the simulations show that an elastic film bonded to a viscous substrate undergoing compression can show two distinct length scales near the threshold. Wrinkles and wrinkle packets emerge near the threshold confirming the scenario given in the Introduction. More importantly, these two distinct modes may appear not necessarily due to specific characteristics of the underlying mechanics, but also due to the randomness of the initial noise. In fact the wrinkle packets observed in the example of Fig. 1B have a different topography than the ones observed in Fig. 3C and D (red color) implying that the initial distribution of amplitudes are not exactly predicted by a uniform distribution.

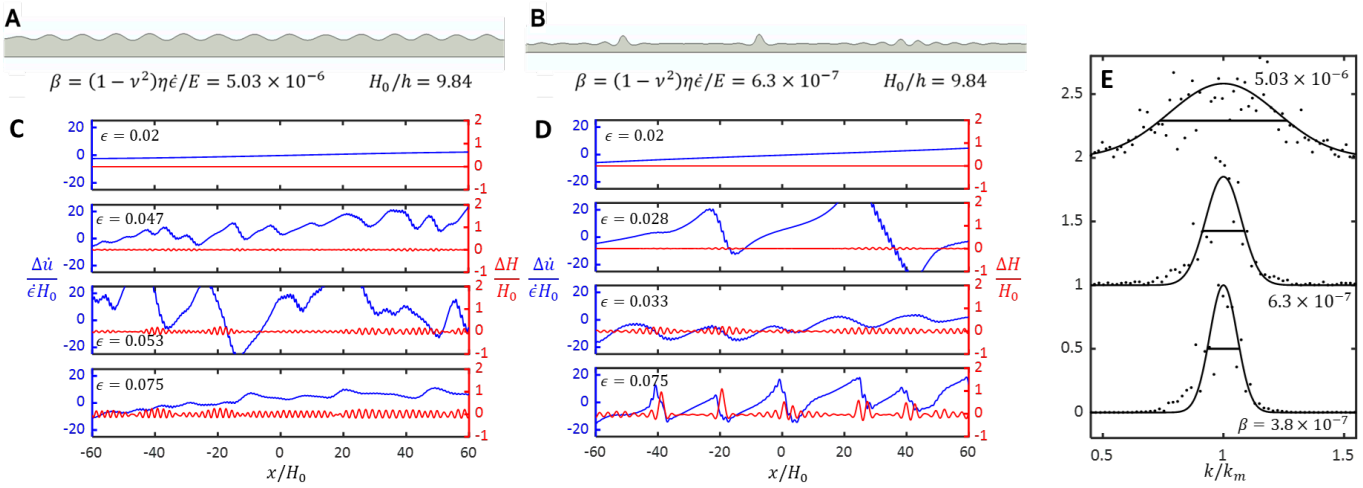

Fig. 3 A&B: Snapshots of buckled geometry at $\varepsilon = 0.075$ for the (A) wrinkling and (B) ridge localization simulations at the β and H_0/h values listed. A wider region is shown for B, making the liquid layer appear thinner. In fact, both have $H_0/h = 9.84$. C&D. Evolution of amplitude (red) and x-velocity (blue) profiles in each simulation. (E) Fourier transform of the amplitude profile at threshold and fits to gaussian (see text) where horizontal lines indicate width of the gaussian. The upper two data are moved vertically by 1 and 2 units respectively.

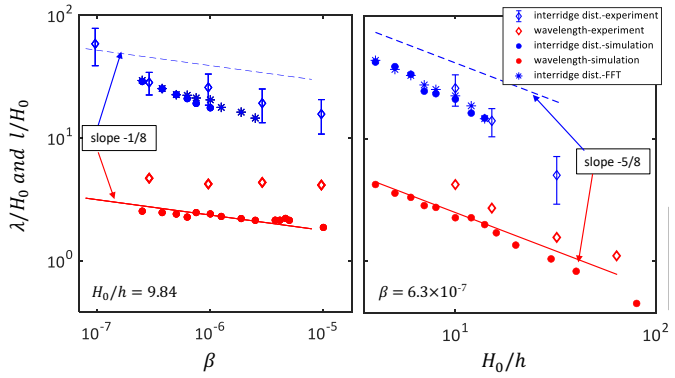

Fig. 4 Dependence of normalized wavelength (red symbols) and interridge distance (blue symbols) on non-dimensional A. rate β, and B. liquid thickness H_0/h. The error bars on the experimental ℓ values indicate the range of distances measured[21]. Error bars on the experimental λ values are smaller than the symbols. The red solid and blue dashed lines correspond to the theoretical predictions in Eqs. (14) and (16), as explained in the text.

3 Theoretical Model

We now seek to understand our system within the framework of previous models that account for the interaction between the film and the fluid. Assuming lubrication approximation for the fluid motion, the dynamics of the film constrained to deformations in the $x-z$ plane is captured by two equations (see ESI†)

$$\partial_t u = -H^2\partial_x p/(2\eta) + H\tau/\eta - \dot{\varepsilon}x \tag{4}$$

$$\partial_t H = \partial_x\left[H^3\partial_x p/(3\eta) - H^2\tau/(2\eta)\right] + \frac{\dot{\varepsilon}}{1-\dot{\varepsilon}t}H \tag{5}$$

The pressure (p) and shear stress (τ) under the film are related to the bending and stretching of the film by $p = B\partial_x^4 H - \partial_x(F\partial_x H)$ and $\tau = \partial_x F$. Here F is the force per unit of width on the cross section that accounts for in-plane elasticity $F = Y\partial_x u$. Equations (4) and (5) were derived by Huang and Suo[6,7] for the case $\dot{\varepsilon} = 0$ (see section 4 for details). Unlike their system however, fluid motion is the driving force deforming the film in our system, and these two extra terms in Eqs. (4) and (5) act as "source terms" that change H and u with time.

Neglecting the stresses in Eqs. (4) and (5) is equivalent to assuming no resistance of the film along the x and z directions. Accordingly, for $p = \tau = 0$, Eq. (3) is a solution to Eqs. (4) and (5) representing homogeneous upward motion of an infinitely long film prescribed by fluid incompressibility, and a compressive strain $\partial_x u = -\varepsilon$ that mirrors the strain of the bottom rubber layer. We devote the next paragraph to understand how this solution arises.

To comprehend how the solution in Eq. (3) emerges, we rely on previous works[20,22] accounting that the equation for the horizontal displacement predicts a "shear-lag" effect. The second term on the right-hand side of Eq. (4) takes the form $H\tau/\eta \approx (H_0 Y/\eta)\partial_x^2 u$, defining a diffusion coefficient $D = H_0 Y/\eta$ and a diffusive time scale $t_D = L^2/D$, where L is the half length of the film (see Fig. 2A). This time scale accounts for the characteristic time required for boundary effects to propagate throughout the system. Therefore, before buckling, spatial and time derivatives are of the order $\partial_x \sim 1/L$ and $\partial_t \sim 1/t_D$. Rescaling horizontal length scales (u, x) with L, vertical length scales with H_0 and time scales with t_D, we make Eqs. (4) and (5) dimensionless (see ESI†). Defining dimensionless quantities by bar symbols, Eqs. (4) and (5) become

$$\partial_{\bar{t}}\bar{u}(\bar{x},\bar{t}) = \bar{H}\partial_{\bar{x}}^2\bar{u} - \varepsilon_D\bar{x} + \mathcal{O}(\Lambda^2,\Lambda^4/N^2)$$

$$\partial_{\bar{t}}\bar{H}(\bar{x},\bar{t}) = -\frac{1}{2}\bar{H}^2\partial_{\bar{x}}^3\bar{u} + \frac{\varepsilon_D}{1-\varepsilon_D\bar{t}}\bar{H} + \mathcal{O}(\Lambda^2,\Lambda^4/N^2) \tag{6}$$

where $\Lambda = H_0/L$ and $\varepsilon_D = \dot{\varepsilon}t_D$ is the strain applied at time t_D. These equations must be solved with the boundary conditions $\bar{u}|_{\bar{x}=0} = 0$ (fix center) and $\partial_{\bar{x}}\bar{u}|_{\bar{x}=\pm1} = 0$ (free ends), and the initial conditions $\bar{u}|_{\bar{t}=0} = 0$ and $\bar{H}|_{\bar{t}=0} = 1$. The approxima-

tion $\bar{H} \approx 1$ in the coupling terms yields the asymptotic solution $\bar{u} = -(\varepsilon_D/2)(\bar{x} - \bar{x}^3/3)$, which is valid for long times ($\bar{t} \gg 1$) when boundary layers formed at the free ends have propagated to the center of the film[20]. Note that this asymptotic solution corresponds to a finite shear $\tau \approx \eta x/H_0$ in dimensional variables. However, here we are interested in the opposite limit when the system size is large ($t_D \to \infty$), and boundary layer effects are negligible. The exact solution for short times of Eqs. (6) is

$$\bar{u}(\bar{x},\bar{t}) = -\varepsilon_D \bar{t}\,\bar{x} + \mathscr{O}(\bar{t}^2); \quad \bar{H}(\bar{x},\bar{t}) = \frac{1}{1-\varepsilon_D \bar{t}} + \mathscr{O}(\bar{t}^2) \quad (7)$$

which is the dimensionless form of Eq. (3). The physical interpretation of the behavior for $t \ll t_D$ is explained by the small magnitude of the elastic forces. Elastic forces are proportional to displacements and substantial deformation is needed to counteract the applied loads represented by the source terms of Eqs. (6). Displacements are on the order of $u \sim t$ at short times, resulting in small elastic forces. Thus, the film deforms in-plane, exactly following the deformation of the bottom rubber for short times, and pressure and shear can be neglected.

We now continue with the analysis of the equations in dimensional variables and use the strain $\gamma = \partial_x u$ as variable to obtain a set of equations invariant under translations. When nonlinear terms involving derivatives of the height ($(\partial_x H)^2$, $\partial_x H \partial_x^2 H$, etc.) are neglected, Eqs. (4) and (5) become

$$\begin{aligned} \partial_t \gamma &= -\frac{1}{2\eta} H^2 [B\partial_x^6 H - Y\partial_x^3(\gamma \partial_x H)] + \frac{Y}{\eta} H \partial_x^2 \gamma - \dot{\varepsilon} \\ \partial_t H &= \frac{1}{3\eta} H^3 [B\partial_x^6 H - Y\partial_x^3(\gamma \partial_x H)] - \frac{Y}{2\eta} H^2 \partial_x^2 \gamma + \frac{\dot{\varepsilon}}{1-\dot{\varepsilon} t} H \end{aligned} \quad (8)$$

We conduct a linear perturbation analysis of these equations around the solution given by Eq. (3), using Fourier modes of the form

$$\begin{aligned} \Delta H/H_0 &= \xi_k(t)\cos(kx) \\ \Delta\gamma &= \omega_k(t)\cos(kx) \end{aligned} \quad (9)$$

where $\Delta\gamma = \partial_x \Delta u = \partial_x u - \partial_x u^{flat}$. This leads to a second order equation for the amplitude of the height perturbation:

$$\ddot{\xi}_k + 2\mu(t,k)\dot{\xi}_k + q^2(t,k)\xi_k = 0 \quad (10)$$

where the functions μ and q are defined in ESI†. Applying the WKB method[25], the general solution for the perturbation amplitude is $\xi_k(t) = (a_1 e^{S_+(t,k)} + a_2 e^{S_-(t,k)})/Q(t,k)^{1/2}$ where $Q^2 = q^2 + (\dot{\mu} + \mu^2)$ and $S_\pm(t,k) = \int_0^t dt'[-\mu(t',k) \pm Q(t',k)]$ are time-dependent growth exponents.

From here on, we use strain instead of time to study the buckle evolution, i.e. we work in terms of $S_\pm(\varepsilon,k)$ rather than $S_\pm(t,k)$. Because $S_- < 0$, the instability appears only when $S_+(\varepsilon,k)$ is positive. As shown in ESI†, for the parameter values of interest, S_+ is well-approximated by the analytical expression

$$S_+(\varepsilon,k) = 2\varepsilon - \varepsilon\frac{(kH_0)^6}{(12\alpha N^2)} + \frac{\varepsilon}{6}(kH_0)^2 + \varepsilon^2\frac{(kH_0)^4}{(24\alpha)} \quad (11)$$

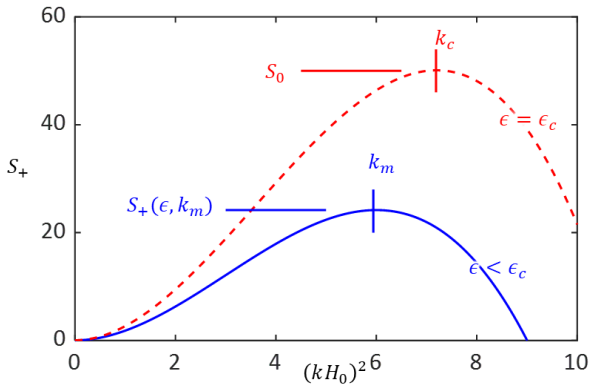

Fig. 5 Evolution of the growth exponent $S_+(\varepsilon,k)$ with increasing strain. Dashed red line corresponds to the strain (and hence time) at which S_+ first reaches a specified value S_0.

To relate this result to classical buckling theory for a free elastic film, we observe that, for very slow compression, ($\alpha \to 0$) the growth function can be approximated as $\alpha S_+/\varepsilon \approx -(kH_0)^6/(12N^2) + \varepsilon(kH_0)^4/24$ where the unstable modes $S_+ > 0$ are obtained when $\varepsilon > 2(kH_0)^2/N^2 = 2Bk^2/Y$. The available modes are determined by boundary conditions, for instance, the Neumann-type boundary condition $\partial_x H|_{x=\pm L} = 0$ yields $k = \pi n/L$ where $n = 1, 2\ldots$ Therefore, the first mode to become unstable as compression increases is $k^{el} = \pi/L$ for $\varepsilon_c^{el} = 2(B/Y)\pi^2/L^2$. The growth function for this mode as strain increases beyond ε_c^{el} is approximately $\alpha S_+(\varepsilon,k^{el})/\varepsilon \approx (\varepsilon - \varepsilon_c^{el})(k^{el}H_0)^4/24$. Thus, the growth of the first unstable mode follows the trend $S_+(\varepsilon,k^{el}) \sim t^2$; however, as shown at the end of this paragraph, there are modes that grow even faster. Figure 5 evaluates S_+ using the parameters of Fig. 3B for illustration. The blue line shows that at any given strain (or equivalently, time), $S_+ > 0$ for small kH_0 indicating an instability. Further, S_+ has maximum at a certain wavenumber k_m which increases with increasing strain. This maximally-unstable wave number can be obtained from $\partial_k(S_+) = 0$ as $(k_m H_0)^2 = \left(N^2\varepsilon + \sqrt{24N^2\alpha + N^4\varepsilon^2}\right)/6$. For a large ratio $\varphi = N\varepsilon/\sqrt{\alpha}$ between the two terms in the square root, we obtain for the maximum

$$(k_m H_0)^2 \approx N^2\varepsilon/3 \quad (12)$$

a strain-controlled but rate-independent regime similar to the scaling law obtained for a film under a fixed prestrain[6] and for filaments immersed in a viscous fluid[8]. In this large strain limit ($\varphi \gg 1$), the evaluation of S_+ gives a simple expression for S_+ at the maximally-unstable wavenumber: $S_+(\varepsilon,k_m) \approx N^4\varepsilon^4/(648\alpha)$. It predicts a super-exponential growth $S_+(\varepsilon,k_m) \sim t^4$ similar to the buckling instability in[8].

Since k_m changes continuously, the instability wavenumber that eventually dominates is the one that sufficiently amplifies an initial small perturbation. We proceed by assuming that the growth exponent must reach $S_+ = S_0 > 1$ to have a significant amplification of perturbations. Here S_0 represents the initial unknown perturbations of the system, $S_0 = \ln(1/A_k)$; however, the precise "amplification criterion" depends on the size of the initial

unknown perturbations of the system and their statistical distribution. A noisier system should require a smaller value for the exponent S_0. Reaching $S_+ \approx S_0$ requires a certain critical strain (dashed red line in Fig. 5). We set $S_0 = N^4\varepsilon^4/(648\alpha)$ to obtain $\varepsilon_c \approx 32^{3/4}(S_0\alpha)^{1/4}/N$ as the critical strain. Note that $\varphi = (648S_0/\alpha)^{1/4}$ at the critical strain. This value is consistently large in all our simulations, thus validating our initial assumption in obtaining Eq. (12).

The critical strain, in terms of our simulation parameters, is

$$\varepsilon_c \approx c_1 S_0^{1/4}\beta^{1/4}(H_0/h)^{-3/4} \tag{13}$$

where $c_1 = 2^{-1/4}3^{1/2} \approx 1.46$. Further, substituting Eq. (13) into Eq. (12) gives the critical wavenumber $(k_cH_0)^2 \approx N^2\varepsilon_c/3 = 2^{3/4}N(S_0\alpha)^{1/4}$, or a critical wavelength

$$\lambda_c/(2\pi H_0) \approx c_2 S_0^{-1/8}\beta^{-1/8}(H_0/h)^{-5/8} \tag{14}$$

where $c_2 = 2^{-7/8}3^{-1/4} \approx 0.41$. Notably, λ_c is very weakly-sensitive to rate and noise (power $1/8$), consistent with the simulations and experiments. Equation (14) is shown as the solid red line in Fig. 4A using the exponent S_0 as fit parameter. It yields $S_0 \approx 30$. We use the same parameter S_0 to predict the relation between wavelength and H_0/h in Fig. 4B (solid red line) and critical strain with β and H_0/h (see ESI†) to show the consistency of our relations. Because the critical strain is more sensitive to initial noise (power $1/4$), the agreement between simulation and theory is less satisfactory. Note that the experimental wavelengths in Fig. 4 always exceed the numerical values suggesting that experiments have higher initial perturbations, and hence need a lower value of S_0.

We remark that Eq. (12) is derived from a linear analysis of Eqs. (8) and its predictions are strictly valid near the threshold. Although it predicts the wavenumber increases with strain for compressions larger than the critical strains ($\varepsilon > \varepsilon_c$), the amplitudes of the unstable modes around k_c increase, and nonlinear terms come into play in the subsequent analysis. In fact, the sequence in Fig. 3C shows that the wavelength of wrinkles changes slowly with compression after threshold. A nonlinear analysis of the equations would be needed to elucidate how the most unstable mode at threshold suppresses the growth of other modes to become dominant.

We now turn to the theoretical analysis of the inter-ridge distance. Unlike ridge localization on elastic substrates where ridges are observed far from threshold[16], Fig. 3B shows that localization appears simultaneously with wrinkling. Moreover, a careful examination of the surface profile near the threshold shows that packets of wrinkles transform into ridges as strain increases, and the distance between the ridges corresponds to the size of these packets. The fourier transform of the profiles near the threshold confirms these observations. We conjecture that these packets of wrinkles add natural imperfections to the film and select the positions where ridges appear. Figure 3C shows that at relatively low β values, the unstable modes have a gaussian-shaped distribution in the region $k_m - k_0 < k < k_m + k_0$. The wavenumber k_0 characterizes the spread of the distribution, which becomes narrower with decreasing rate. It is well-known[29] from fourier analysis that a gaussian distribution of modes predicts the appearance of wave packets with a size $\sim k_0^{-1}$. Physically, these wave packets appear because modes within $\pm k_0$ of k_m beat with each other to create wave packets at a spacing of order $\sim 1/k_0$. Thus, the long wavelength or inter-ridge distance is a modulation of the profile rather than a new distinct sinusoidal undulation.

The same conclusion is supported by the analysis of the growth function. Figure 5 shows that there is a band of rapidly growing modes for $\varepsilon > \varepsilon_c$ defined by the condition $S_+ > S_0$. Specifically, near the maximum the growth function can be approximated as $S_+(\varepsilon,k) \approx S_+(\varepsilon,k_m) - (k-k_m)^2/k_0^2$, where

$$(k_0H_0)^2 \approx 18\alpha/(N^2\varepsilon^3) \tag{15}$$

It predicts that the fourier distribution given by the solution $\xi_k(t) \propto e^{S_+}$ has a gaussian shape centered at k_m with width k_0. Equation (15) is strongly different than Eq. (12). It shows that the size of a wave packet depends on strain rate in agreement with Fig. 4C.

To connect k_0 with the inter-ridge distance, we use the analysis of Eq. (2). For constant initial perturbations A_k there are wrinkle packets of the form $\xi \sim e^{-x^2/2\sigma^2}$ where $\sigma = \sqrt{2}/k_0$[29]. Taking the inter-ridge distance as $\ell = 4\sigma$ (equivalent to two standard deviations in a gaussian distribution, see Fig. 1A), we now estimate ℓ in our Abaqus simulations by performing Fourier analysis on the amplitude profiles and fitting them to a Gaussian-shaped distribution to obtain k_0, as shown in Fig. 3E. Figure 4 (blue star points) shows that this method gives similar ℓ values as the analysis of the spatial autocorrelation functions (see ESI†, section S3). However, at high rates, Fourier analysis cannot be used because noisy data result in poor-quality Gaussian fits. Note that this data analysis includes the unknown initial distribution of amplitudes in numerical simulations explained by roundoff errors and discretization. This distribution could shift the values of k_c and k_0 predicted by theory assuming a uniform distribution (or white noise) of the initial amplitudes. Indeed, as we analyze below, the gaussian distributions observed in Fig. 3E show a deviation from the theoretical predictions obtained under these simple assumptions.

Although Eqs. (12) and (15) describe two different length scales, they are connected at threshold when assuming that the initial amplitude perturbations do not play a role in predicting k_c or k_0. Their ratio $k_c^2/k_0^2 = N^4\varepsilon_c^4/(54\alpha)$ is proportional to the growth exponent. It yields $k_c^2/k_0^2 = 12S_0$ at the threshold condition. Equivalently, the ratio between the inter-ridge distance and wavelength is then

$$\ell/\lambda_c = (96S_0/\pi^2)^{1/2} \tag{16}$$

Thus, the inter-ridge distance is just a multiple of the wavelength! Indeed Fig. 4 shows that ℓ/λ_c is almost independent of liquid thickness, and only weakly dependent on rate. Quantitatively, we obtain $\ell \approx 17\lambda_c$ for $S_0 \approx 30$ (upper dashed blue line), which is in reasonable agreement with the experiments and simulations. The difference shows that Eq. (15), or equivalently Eq. (16) at threshold, under-predicts the k_0 values extracted directly from the fourier transform (blue star points in Fig. 4). Therefore, there is a wider distribution than the theoretical prediction implying that

the initial distribution of amplitudes is not uniform.

4 Other Systems

The same analysis can be applied to similar problems where viscous forces are dominant to buckle a filament or film. The instability analysis will lead to a growth function where the most unstable mode k_m and the width of the gaussian distribution k_0 can be extracted. Although, the previous analysis predicts $\lambda \approx 2\pi/k_m$ and $\ell \approx 4\sqrt{2}/k_0$ these relations are approximate because the magnitudes of the amplitudes and their statistical distribution are important to exactly predict the critical strain for buckling, wavelength at threshold, and the corresponding band width of unstable modes. However, k_m and k_0 give a first estimation of the topography of the wrinkle packets and the behavior of natural imperfections after buckling.

The results thus far have only examined the case when the film experiences continuous compression at a fixed rate $\dot{\varepsilon}$. But the same approach can be applied to the case where a sudden compression of strain ε_0 is applied to a film supported by a viscous fluid. This instantaneous compression could be applied to the film by thermal effects, swelling, pre-stretching release, etc. The same setup defined in Fig. 2 can be used to study the effect of a sudden compression if the rubber bottom is released sufficiently fast. We have reported that wrinkling is observed during the first stage of fast compression, whereas localized ridges appear under quiescent conditions after the strain has been applied[21].

Previous studies[4–7] have computed the instability for this type of compression and only predicted uniform wrinkles. The instantaneous compression dictates a constitutive relation $F = Y(\partial_x u - \varepsilon_0)$ so that the force is initially compressive for small displacement ($F \approx -Y\varepsilon_0$) and relaxation takes place after a time t_D ($F \approx 0$). Equations (4) and (5), without source terms and with this new constitutive relation, describe the dynamics of the film. In terms of the strain $\gamma = \partial_x u$ and height H the equations to solve are

$$\partial_t \gamma = -\frac{1}{2\eta} H^2 [B\partial_x^6 H - Y\partial_x^3((\gamma-\varepsilon_0)\partial_x H)] + \frac{Y}{\eta} H \partial_x^2 \gamma$$

$$\partial_t H = \frac{1}{3\eta} H^3 [B\partial_x^6 H - Y\partial_x^3((\gamma-\varepsilon_0)\partial_x H)] - \frac{Y}{2\eta} H^2 \partial_x^2 \gamma \quad (17)$$

Before buckling we expect again that spatial and time derivatives scale in the form $\partial_x \sim 1/L$ and $\partial_t \sim 1/t_D$. Rescaling the variables in the same way we did in the previous problem, we make the equations dimensionless. Equations (17) become

$$\partial_{\bar{t}} \gamma(\bar{x},\bar{t}) = \bar{H}\partial_{\bar{x}}^2 \gamma + \mathscr{O}(\Lambda^2, \Lambda^4/N^2)$$

$$\partial_{\bar{t}} \bar{H}(\bar{x},\bar{t}) = -\frac{1}{2}\bar{H}^2 \partial_{\bar{x}}^2 \gamma + \mathscr{O}(\Lambda^2, \Lambda^4/N^2) \quad (18)$$

They must be solve with the boundary conditions $\gamma|_{\bar{x}=\pm 1} = \varepsilon_0$ (free ends) and the initial conditions $\gamma|_{\bar{t}=0} = 0$ and $\bar{H}_{\bar{t}=0} = 1$. The solution for short times ($t \ll t_D$) is $\gamma = 0 + \mathscr{O}(\bar{t}^2)$ and $\bar{H} = 1 + \mathscr{O}(\bar{t}^2)$. Thus, a linear stability analysis around this solution provides the specific growth function for large systems. It yields (see ESI†)

$$S = \frac{1}{12}\left(\varepsilon_0 - \frac{(kH_0)^2}{N^2}\right)(kH_0)^4 t_* \quad (19)$$

where t_* is a dimensionless time defined by $t_* = Yt/(\eta H_0)$. Minimization with respect to the wavenumber shows that the equivalent to Eqs. (12) and (15) are

$$(k_m H_0)^2 \approx 2N^2\varepsilon_0/3 \quad (20)$$

$$(k_0 H_0)^2 \approx 9/(2\varepsilon_0^2 N^2 t_*) \quad (21)$$

Thus, the gaussian becomes narrower with time. The ratio $k_m^2/k_0^2 = 4\varepsilon_0^3 N^4 t_*/27$ increases with time, predicting that wrinkle packets should start to separate more and more as time increases[21,30]. Because the strain is fixed, k_m does not change with time, and hence $k_c = k_m$; however, there is a critical time when the growth function reaches the threshold value $S(t_*, k_m) = S_0$. It yields $t_{*c} \approx 81 S_0/(\varepsilon_0^3 N^4)$. In dimensional terms $t_c \sim (9/16)(S_0\eta/Y)(\varepsilon_0 H_0/h)^{-3}$. Accordingly, the time needed to observe the wrinkling instability is expected to increase sharply as the strain or liquid thickness reduces.

Another situation is the compression of a filament immersed in a viscous fluid due to thermal expansion, swelling or other mechanism. It produces a homogeneous compression similar to the compression applied by shear flow in the previous examples. In fact, when thermal expansion or swelling is induced at a constant rate by a linear change with time, it defines an effective compression rate $\dot{\varepsilon}$ (see ESI†). The main source of dissipation is the Stokes flow around the filament and viscous force per unit of line can be readily estimated[8,31] as $\vec{F}_d = -\mu\vec{v}$ where $\mu \propto \eta$. Although the computation of the drag force $\vec{F}_d$ requires a 3D analysis of the flow around the filament, we constrain the motion to take place in the plane $x-z$ so that $\vec{v} = (\partial_t u, \partial_t H)$. The drag force can be divided into normal (T_n) and frictional (T_t) components (similar to p and τ in the previous problem) so that $\vec{F}_d = -T_t\hat{x} + T_n\hat{z}$. These two forces per unit of line are related to bending and stretching of the filament by $T_n = EI\partial_x^4 H - \partial_x(F\partial_x H)$ and $T_t = \partial_x F$, where I is the moment of inertia and F is the tangential force in the cross section. The constitutive relation for in-plane deformation is $F = EA(\gamma - \dot{\varepsilon}t)$ where $\gamma = \partial_x u$; hence, the dynamic of the filament can be reduced to two equations

$$\mu\partial_t \gamma = EA\partial_x^2 \gamma$$

$$\mu\partial_t H = -EI\partial_x^4 H + EA\partial_x((\gamma - \dot{\varepsilon}t)\partial_x H) \quad (22)$$

Because of the simplicity of the viscous forces the diffusive equation for the horizontal displacement becomes decoupled from the vertical displacement. The diffusion equation must be solved with the boundary conditions $\gamma|_{x=\pm L} = \dot{\varepsilon}t$ (free ends) and the initial conditions $\gamma|_{t=0} = 0$. The diffusion coefficient is now $D = EA/\mu$ and the solution for short times ($t \ll t_D$) is $\gamma = 0$ and $H = H_0$. A linear stability analysis around this solution yields for the growth function

$$S = \frac{1}{\mu}\left(-EIk^4 t + EA\dot{\varepsilon}k^2\frac{t^2}{2}\right) \quad (23)$$

The most unstable mode and spread of the gaussian are then

$$k_m^2 = A\varepsilon/(4I) \tag{24}$$

$$k_0^2 = 4\pi\eta\dot{\varepsilon}/(EA\varepsilon^2) \tag{25}$$

Moreover, the same analysis used in the previous section leads to the determination of the critical strain, critical wavenumber and size of the wave packets at threshold. It remains to be studied if nonlinear terms, due for example to the proximity of a solid wall, allow these imperfections to develop into regions of high local curvature.

Other buckling instabilities in fluid-structure interactions, such as indentation of floating films, deflation of shells or real cells immersed in viscous fluid, deformation of microtubules by molecular motors, etc. could also show a small band width of unstable modes leading to the phenomena of beating. Thus, natural imperfections with long scale modulations in the form of wrinkle packets must be observable at threshold and potentially trigger localization.

5 Conclusions

A key dimensionless parameter introduced in the analysis for constant strain rate compression is the ratio of film stiffness to an effective substrate stiffness, $E/(\eta\dot{\varepsilon}) \propto \beta^{-1}$. This implies that low and high compression rate regimes are equivalent to low and high viscosity respectively. Thus, low viscosity or slow compression is necessary to allow rapid fluid motion over large distances to permit the amplification of the wave packets set up at threshold. In this regard, an "instantaneous" compression of the film in a strain-controlled system corresponds to a very small value of the effective mismatch $E/(\eta\dot{\varepsilon})$, thus preventing localization. Yet, after compression, the system can be regarded as having an almost zero strain rate, and localization must be observed for sufficiently long times as observed experimentally under quiescent conditions[21,30].

The concept of an effective mismatch ratio may be useful in guiding research and predicting how other situations of buckling in fluid-structure interactions translate when viscous forces become important and imperfections in the form of packets of wrinkles are developed. There are two necessary conditions to develop localization: 1) a sufficiently large system to include a number of wrinkle packets and neglect relaxation at the boundaries, and 2) slow compression (or equivalently, small values of β) to buckle the structure along the direction dictated by large scale imperfections. However, nonlinear terms play a fundamental role to amplify or suppress localization. We expect that the proximity of a solid wall facilitates amplification by decreasing the vertical mobility with respect to the horizontal mobility and hence preventing downward vertical movement of the film.

This research was supported by NSF-CMMI-1636064, NSF-CMMI-561789, and NIH R56-HL142743-01. EC acknowledges the support of Fondecyt Grant No 1201250. LP and NN acknowledge the support of NIH R01-HL159205-01.

Notes and references

1 C. Pallavicini, A. Monastra, N. González Bardeci, D. Wetzler, V. Levi, and L. Bruno, *European Biophysics Journal*, 2017, **46**, 581.
2 W. Gilpin, M.S. Bull, and M. PraKash, *Nature Reviews Physics*, 2020, **2**, 74.
3 S.T. Nabavi and H. Fossen, *Earth-Science Reviews*, 2021, **222**, 103812.
4 N. Sridhar, D. J. Srolovitz, and Z. Suo, *Applied Physics Letters*, 2001, **78**, 2482.
5 J. Liang, R. Huang, H. Yin, J. C. Sturm, K. D. Hobart, and Z. Suo, *Acta Materialia*, 2002, **50**, 2933.
6 R. Huang and Z. Suo, *Journal of Applied Physics*, 2002, **91**, 1135.
7 R. Huang and Z. Suo, *International Journal of Solids and Structures* 2002, **39**, 1791.
8 J. Chopin, M. Dasgupta and A. Kudrolli, *Phys. Rev. Lett.*, 2017, **119**, 088001.
9 B. Li, Y.P. Cao, X.Q. Feng, and H. Gao, *Soft Matter*, 2012, **8**, 5728.
10 Q. Wang and X. Zhao, *J. Applied Mechanics*, 2014, **81**, 051004.
11 N. Bowden, S. Brittain, A. G. Evans, J. W. Hutchinson, and G. M. Whitesides, *Nature*, 1998, **393**, 146.
12 F. Brau, H. Vandeparre, A. Sabbah, C. Poulard, A. Boudaoud, and P. Damman, *Nature Physics*, 2011, **7**, 56.
13 Y. Cao and J. W. Hutchinson, *Journal of Applied Mechanics-Transactions of the Asme*, 2012, **79**, 031019.
14 A. Takei, L. Jin, J. W. Hutchinson, and H. Fujita, *Advanced Materials*, 2014, **26**, 4061.
15 C. Cao, H. F. Chan, J. Zang, K. W. Leong, and X. Zhao, *Advanced Materials*, 2014, **26**, 1763.
16 A. Auguste, J. W. Yang, L. H. Jin, D. Y. Chen, Z. G. Suo, and R. C. Hayward, *Soft Matter*, 2018, **14**, 8545.
17 H. Diamant and T. A. Witten, *Phys. Rev. Lett.*, 2011, **107**, 164302.
18 V. Demery, B. Davidovitch, and C. D. Santangelo, *Phys. Rev. E*, 2014, **90**, 042401.
19 D. Vella, J. S. Huang, N. Menon, T. P. Russell, and B. Davidovitch, *Phys. Rev. Lett.*, 2015, **114**, 014301.
20 S. Chatterjee, C. McDonald, J. Niu, S. S. Velankar, P. Wang, and R. Huang, *Soft Matter*, 2015, **11**, 1814.
21 X. Guan, A. P. Sarma, E. Hamesh, J. Yang, N. Nguyen, E. Cerda, L. Pocivavsek, and S.S. Velankar, *Int. J. Solids Struct.*, **254-255** 111843.
22 X. Guan, A. N. Nguyen, L. Pocivavsek, E. Cerda, and S.S. Velankar, *Int. J. Solids Struct.*, 2023, **275**, 112242.
23 K.O. Mikaelian, *Phys. Rev. Lett.*, 1998, **80**, 508.
24 R. Serway and J. Jewett, Physics for Scientists and Engineers (Brooks/Cole-Thomson Learning, Belmont, 2004)
25 D.J. Griffiths and F. Schroeder, in Introduction to Quantum Mechanics (Cambridge University Press, Cambridge, 2018).
26 S. Mane and R. Huang, *Int. J. Solids Struct.*, 2022, **257**, 111592.
27 J. Zavodnik, A. Kosmrlj, and M. Brojan, *J. Mech. Phys. Solids*,

2023, **173**, 105219.
28 X. Liu, Y. Liu, and X.Q. Feng, *Int. J. Solids Struct.*, 2022, **249**, 111689.
29 A. L. Fetter and J. D. Walecka, in Theoretical Mechanics of Particles and Continua (Dover Publications, New York, 2003).
30 X. Guan, Compression rate-dependent buckling and creasing mechanics of elastic and viscoelastic films. (University of Pittsburgh. Ph.D. thesis, 2022).
31 T. R. Powers, *Rev. Mod. Phys.*, 2010, **82**, 1607-1631.